

Batteries

International Edition: DOI: 10.1002/anie.201910916
German Edition: DOI: 10.1002/ange.201910916

A Pyrazine-Based Polymer for Fast-Charge Batteries

Minglei Mao, Chao Luo,* Travis P. Pollard, Singyuk Hou, Tao Gao, Xiulin Fan, Chunyu Cui, Jinming Yue, Yuxin Tong, Gaojing Yang, Tao Deng, Ming Zhang, Jianmin Ma, Liumin Suo, Oleg Borodin,* and Chunsheng Wang*

Abstract: The lack of high-power and stable cathodes prohibits the development of rechargeable metal (Na, Mg, Al) batteries. Herein, poly(hexaazatrinaphthalene) (PHATN), an environmentally benign, abundant and sustainable polymer, is employed as a universal cathode material for these batteries. In Na-ion batteries (NIBs), PHATN delivers a reversible capacity of 220 mAh g^{-1} at 50 mA g^{-1} , corresponding to the energy density of 440 Wh kg^{-1} , and still retains 100 mAh g^{-1} at 10 A g^{-1} after 50 000 cycles, which is among the best performances in NIBs. Such an exceptional performance is also observed in more challenging Mg and Al batteries. PHATN retains reversible capacities of 110 mAh g^{-1} after 200 cycles in Mg batteries and 92 mAh g^{-1} after 100 cycles in Al batteries. DFT calculations, X-ray photoelectron spectroscopy, Raman, and FTIR show that the electron-deficient pyrazine sites in PHATN are the redox centers to reversibly react with metal ions.



Introduction

Lithium-ion batteries (LIBs) are the dominant power supply for the portable electronics, electric vehicles, and grid-scale energy-storage systems because of the high energy density and stable cycling performance.^[1] However, the large-scale application of LIBs is constrained by the limited and unevenly distributed lithium resources in the Earth's crust.^[2] NIBs are promising alternatives to LIBs, owing to the abundance, low cost of Na sources, comparable potential to Li (-2.71 V for Na/Na^+ vs. -3.04 V for Li/Li^+),^[3] and the similar chemistry between NIBs and LIBs.^[4] However, the energy densities of NIBs are intrinsically limited by their intercalation chemistry.^[5] To break this limitation, multivalent rechargeable Mg (RMBs) and Al (RABs) batteries have attracted considerable research interests, owing to the high

volumetric energy density, high abundance, and less reactivity in ambient atmosphere of Mg and Al metal.^[6] More importantly, the dendrite-free stripping/plating process of Mg metal avoids the safety concern from the internal short-circuit of rechargeable batteries, and ensures long-term cycling stability.^[7] All these merits make RMBs and RABs promising candidates for consumer electronics applications, where volumetric energy density and safety are priority.

The cathode materials are the energy-limiting components for NIBs,^[3] RMBs,^[8] and RABs.^[9] For example, expensive transition-metal (such as Co and Ni) oxides for NIBs can only provide the capacities of about 150 mAh g^{-1} . Moreover, they cannot be used in RMBs and RABs, because the strong interaction of Mg^{2+} and Al^{3+} with the host materials leads to sluggish intercalation kinetics.^[10] Up to now, Chevrel-phase Mo_6S_8 is still the most successful cathode for RMBs and RABs,^[11] which, however, suffers from low energy densities. To circumvent these challenges, metal-free polymer materials, with the advantages of light weight, abundance, low cost, and recyclability, stand out as the universal cathodes for NIBs,^[12] RMBs,^[13] and RABs,^[13a,b] because the flexible structural tunability, weak intermolecular force and interaction with insertion cations facilitate the reaction kinetics.^[14] Among various organic materials, organosulfur compounds,^[15] organic free-radical compounds,^[16] carbonyl compounds,^[17] imine compounds,^[18] and azo compounds^[19] have been explored as electrodes for batteries. However, low redox stability, high solubility in electrolyte, and low electronic conductivity remain crucial limitations to the application of these compounds.^[20] Polymerizing the redox-active compounds has been demonstrated as an effective way to suppress the dissolution of the organic electrodes and increase the intrinsic electrical conductivity.^[20b,21] Introducing heteroatoms (O, N, and S) with a lone

[*] Dr. M. Mao, S. Hou, Dr. T. Gao, Dr. X. Fan, C. Cui, T. Deng,

Prof. C. Wang
Department of Chemical and Biomolecular Engineering
University of Maryland
College Park, MD 20742 (USA)
E-mail: cswang@umd.eduProf. C. Luo
Department of Chemistry and Biochemistry
George Mason University
Fairfax, VA 22030 (USA)
E-mail: cluo@gmu.eduDr. M. Mao, C. Cui, Prof. M. Zhang, Prof. J. Ma
State Key Laboratory of Chemo/Biosensing and Chemometrics,
School of Physics and Electronics, Hunan University
Changsha 410082 (China)Dr. M. Mao, J. Yue, Y. Tong, G. Yang, Prof. L. Suo
Key Laboratory for Renewable Energy, Beijing Key Laboratory for New
Energy Materials and Devices, Beijing National Laboratory for
Condensed Matter Physics, Institute of Physics
Chinese Academy of Sciences
Beijing 100190 (China)T. P. Pollard, Dr. O. Borodin
Electrochemistry Branch, Power and Energy Division Sensor and
Electron Devices Directorate, US Army Research Laboratory
Adelphi, MD 20783 (USA)
E-mail: oleg.a.borodin.civ@mail.mil Supporting information and the ORCID identification number(s) for
the author(s) of this article can be found under:
 <https://doi.org/10.1002/anie.201910916>

pair of electrons into organic materials to form π -conjugated aromatic compounds can achieve multiple redox centers and enhance the intrinsic electrical conductivity.^[22] Besides, high-concentration electrolytes are also reported to be effective in suppressing the dissolution and improving the cycling stability of polymer electrodes.^[23]

Hexaazatrinaphthalene (HATN; Supporting Information, Figure S1b), which is an electron-deficient, rigid and planar aromatic discotic system with imine functional groups, has been investigated as cathode materials for LIBs and supercapacitors.^[24] Although having a high theoretical capacity of 418 mAh g^{-1} , HATN suffers from high solubility and poor cycling stability.^[24,25] Introducing 1,4-bisethynylbenzene as a linker between HATN cores only slightly enhances the cycling stability and rate capability.^[26] Polymerizing HATN (PHATN) (Supporting Information, Figure S1c) will reduce its solubility in electrolyte and obtain high electrical conductivity.^[27] In this work, we discover that PHATN can be used as a high rate and stable cathode material in third-period metal (Na, Mg, and Al) batteries. In NIBs, PHATN achieves fast reaction kinetics, ultra-stable cycling stability, and high energy density. In RMBs and RABs, PHATN also displays stable cycling performance and fast reaction kinetics. For the first time, we proved that a pyrazine derivative can be used as cathodes in multivalent Mg and Al batteries, and the excellent electrochemical performance of PHATN for NIBs, RMBs, and RABs demonstrate that pyrazine-based polymers are promising universal cathodes for sustainable rechargeable batteries.

Results and Discussion

Ion storage mechanism of PHATN

PHATN, in which HATN is linked via a carbon–carbon bond between two phenyl rings, was synthesized by a condensation reaction between cyclohexanone and amines, according to a previously reported procedure with some modifications.^[27b] PHATN particles are amorphous (Supporting Information, Figure S3a) and degraded only above 100°C (Supporting Information, Figure S3b). The existence of $\text{C}=\text{N}$ redox-active center in PHATN is confirmed by the peak at 1495 cm^{-1} in FTIR (Supporting Information, Figure S3c).^[27b]

PHATN was first evaluated as the cathode for NIBs in coin cells, which delivers initial discharge/charge capacities of 236 and 251 mAh g^{-1} , respectively (Figure 1a). The initial coulombic efficiency (CE) is slightly above 100% owing to the formation of cathode electrolyte interface (CEI) of PHATN, which is common in the polymer electrode.^[12b,20c,26] At high voltage ($3.5 \text{ V vs. Na/Na}^+$), a cathode–electrolyte interphase (CEI) layer forms, mainly resulting from the complicated chemical/electrochemical surface reaction between PHATN and electrolyte (with some unavoidable impurity and water). In the 2nd and 3rd cycles, the CE is close to 100% and the reversible capacity remains at around 220 mAh g^{-1} , corresponding to three Na^+ coordinated with electroactive pyrazine N atoms. The discharge/charge curves exhibit a short shoulder at around 2.5 V and a long slope at

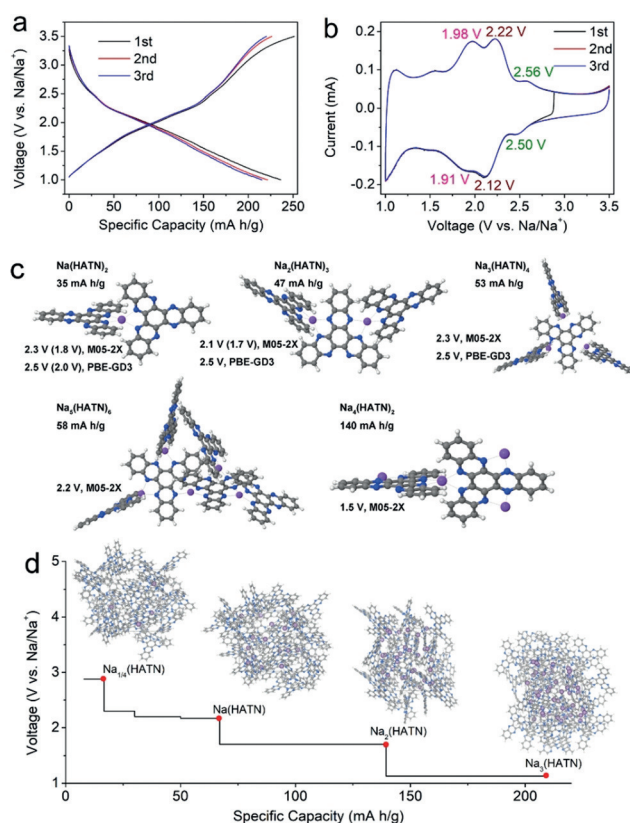


Figure 1. Electrochemical performance of PHATN with a $4 \text{ M NaPF}_6/\text{DME}$ electrolyte between 1 and 3.5 V and predicted insertion potential of PHATN in NIBs. a) Discharge–charge curves of PHATN for the first three cycles at 50 mA g^{-1} . b) Cyclic voltammograms of PHATN at a scan rate of 0.5 mV s^{-1} . c) Optimized geometries and insertion potentials vs. Na/Na^+ of the $\text{Na}_m(\text{HATN})_n$ complexes surrounded by implicit solvent from DFT calculations using M05-2X/6-31 + G(d,p) and PBE-GD3/6-31 + G(d,p) DFT calculations. d) Discharge voltage profile from DFT calculations using Perdew–Burke–Ernzerhof functional with Grimme dispersion correction (PBE-D3) for $\text{Na}_m(\text{HATN})_n$ model cathodes with a Na:HATN ratio from 1:8 (ca. 8 mAh g^{-1}) to 3:1 (ca. 200 mAh g^{-1}). Insets: snapshots of the $\text{Na}_m(\text{HATN})_n$ optimized geometries from DFTB calculations corresponding to material compositions. Na violet. Images prepared with VESTA.^[28]

$1.5\text{--}2.4 \text{ V}$. The multi-step redox reaction of PHATN is confirmed by CV, which displays three pairs of peaks at $2.5 \text{ V}/2.56 \text{ V}$, $2.12 \text{ V}/2.22 \text{ V}$, and $1.91 \text{ V}/1.98 \text{ V}$ (Figure 1b).

The mechanism for metal-ion insertion into PHATN was theoretically investigated. The redox potential can be calculated using density functional theory (DFT) calculations.^[29] Two types of DFT calculations are used to examine redox properties of the PHATN organic cathodes at molecular levels. In the first type of calculation, $\text{M}(\text{HATN})_n$ ($\text{M} = \text{Na, Mg}$) clusters are immersed in a polarized continuum, and their reduction, oxidation and energies of the metal-ion transfer from the metal anode to $\text{M}(\text{HATN})_n$ cathode are calculated. In the second type of calculations, PHATN is packed in a periodic cell and relaxed. A more computationally efficient (by 1–3 orders of magnitude) density functional tight binding (DFTB) method is used in order to obtain representative configurations of the amorphous cathode, while DFT is used for calculating energies for the metal-ion

transfer from metal anode to cathode. Owing to strong binding of Mg and Al to PHATN, it is challenging to obtain equilibrated cathode structures as it requires overcoming large barriers during equilibration, thus we only primarily utilize these calculations for understanding PHATN cathodes in NIBs.

We first calculated reduction potential of the HATN monomer surrounded by implicit solvent, using ether solvent parameters and continuum polarizable conductor model (CPCM) as implemented in Gaussian g16 software.^[30] Reduction potentials of HATN vary from 1.4 V to 2.1 V vs. Na/Na⁺ (Supporting Information, Table S1) depending on the functional and solvation model. The CPCM model together Perdew–Burke–Ernzerhof functional with the Grimme dispersion correction (PBD-D3) yields a value of 2.2 V vs. Na/Na⁺. Using a hybrid DFT functional with a significant 56 % of Hartree–Fock (HF) exchange, M05-2X yields circa 0.3 V lower reduction potential. Lowest unoccupied molecular orbital (LUMO) of HATN is centered on nitrogen atoms and central ring of HATN (Supporting Information, Figure S5a). The complexation of PHATN with metal ions, however, polarizes PHATN and results in a shift of LUMO and highest occupied molecular orbital (HOMO) towards the metal cation as shown for Mg(HATN)₂ complex in the Supporting Information, Figure S5b,c.

DFT calculations were also used to investigate the influence of sodiation on the band gap of the material (Supporting Information, Table S2). Hybrid functionals PBE0 and M05-2X predict the HATN monomer to have a sizeable band gap of 3.98 eV and 5.74 eV, respectively. Upon sodiation, both functionals predict a reduction in the band gap by > 3 eV for Na(HATN)₂ and Na₂(HATN) clusters. We see this reduction for the amorphous solid as well, where, owing to the computational cost, the PBE functional is used instead of PBE0 or M05-2X. Self-polarization through π – π stacking leads to a reduction in the band gap relative to the gas phase monomer from about 2.1 eV to about 1.2 eV. Upon sodiation, this gap vanishes at capacities as low as 8 mAh g^{−1} [Na(HATN)₈]. While we do not expect PBE to accurately capture the magnitude of the band gap, the trend of it narrowing with intercalation is consistent with cluster calculations using more accurate functionals and translates to an increased electronic conductivity.

Reduction and oxidation potentials of Na(HATN)₂ surrounded by CPCM implicit solvent were found at 2.02 V and 2.34 V vs. Na/Na⁺ from PBE-D3/6–31 + G(d,p) DFT calculations. These values are within 0.3 V of the reduction of HATN monomer surrounded by CPCM, indicating a commonly used screening of monomer reduction potential is reflective of the organic cathode redox potential.^[29] When SMD (ether) solvation model is used, the charge states become less favorable compared to CPCM model, resulting in the lower reduction potential to 1.70 V and increased oxidation potential to 2.49 V (Supporting Information, Table S3). This suggests that the Na(HATN)₂ complex at the cathode surface in contact with electrolyte are likely to reduce at a slightly lower potential and oxidize at slightly higher potential than Na(HATN)₂ in bulk of cathode.

The energy of Na transfer from Na metal anode to Na(HATN)₂ complex surrounded by CPCM model was estimated to be 2.76 and 2.22 V vs. Na/Na⁺ from DFT calculations using PBE-D3 and M05-2X functionals, respectively. The potentials in the Supporting Information, Table S3 that were calculated using SMD (ether) solvation model are similar to the measured discharge potentials shown in Figure 1a. Increasing the Na to HATN ratio accompanied with the capacity increase from 35 mAh g^{−1} to 53 mAh g^{−1} does not change redox potential (Figure 1c). Further capacity increase to 140 mAh g^{−1} leads to drop of redox voltage to 1.5 V vs. Na/Na⁺ (Figure 1c). A good agreement is found between the redox potentials from DFT calculations in Figure 1d and experimental results in Figure 1a. Slightly higher redox potentials from DFT calculations are likely owing to potential polarization in galvanostatic discharge and their overestimation by PBE-D3 functional, which predicts higher reduction potential and redox potential compared to hybrid M05-2X functional shown in the Supporting Information, Tables S1 and S2. The inset of Figure 1d shows the optimized geometries of Na_m(HATN)_n model cathodes with a Na: HATN ratio from 1:8 (ca. 8 mAh g^{−1}) to 3:1. The redox potentials of Mg(HATN)₂ were also estimated from the similar DFT calculations using CPCM model except using a larger aug-cc-pvTz basis set, in which PHATN yields redox potentials of 1.20 V vs. Mg/Mg²⁺ (Supporting Information, Table S4).

Sodiation and De-sodiation Performance of PHATN

The electrochemical performance of PHATN for Na batteries is further investigated with 4M NaPF₆/DME electrolyte in coin cells. Along with a high capacity of > 200 mAh g^{−1} (Figure 1a), PHATN also exhibits excellent rate capability and cycle stability (Figure 2). As the current densities increase from C/8 to 5C, capacities show a small decline from 220 mAh g^{−1} to 164 mAh g^{−1}. Even at high current densities of 12C and 25C, PHATN still retains the reversible capacities of 138 and 105 mAh g^{−1}, respectively, indicating the fast reaction kinetics during sodiation and de-sodiation process. The high capacity and superior rate performance contribute to the high energy density and power density. PHATN delivers an energy density of 210 Wh kg^{−1} at the ultrahigh power density of 20000 W kg^{−1}, which is highly competitive to most previously reported organic cathodes for NIBs (Figure 2b).^[31] In addition to high energy and power density, PHATN also shows excellent cycling stability. At 50 mA g^{−1} (C/8), it delivers a reversible capacity of 205 mAh g^{−1} after 100 cycles (Supporting Information, Figure S6a). Under 2 A g^{−1} (5C), it delivers a capacity of 165 mAh g^{−1} after 10000 cycles, with a capacity retention of 89.2 % (Figure 2c). Further increasing the current density to 10 A g^{−1} (25C), PHATN still retains a capacity of 100 mAh g^{−1} after an ultra-long 50000 cycles with a capacity retention of 83.8 % (Figure 2d). To the best of our knowledge, these capacity delivery and retention are the highest among both polymer and inorganic cathodes reported for NIBs.^[12a,19b,22a,c,31a,b] Several dissolution experiments of pristine, discharged, and cycled PHATN in NIBs electrolyte (4M NaPF₆/DME) were performed (Supporting

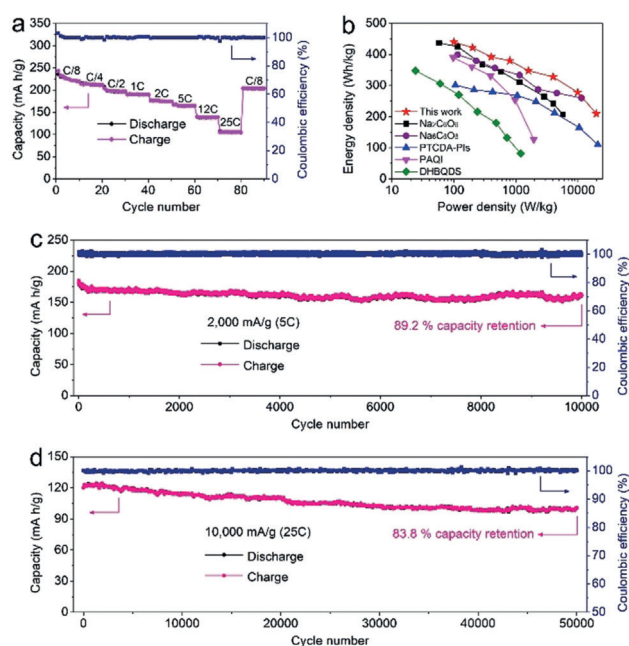


Figure 2. Electrochemical performance of PHATN with a 4 M NaPF₆/DME electrolyte between 1 and 3.5 V for Na batteries. a) Rate capability at various current density from C/8 to 25 C. b) Comparison of energy density and power density between PHATN (this work) and other organic cathodes for Na batteries. c,d) Long-term cycling performance of PHATN under the current densities of 2 Ag⁻¹ (5C) and 10 Ag⁻¹ (25C) for 10 000 and 50 000 cycles, respectively. The capacity retention of PHATN is 89.5 % and 83.8 % after 10 000 and 50 000 cycles, respectively.

Information, Figure S7c), in which all the solutions keep transparent, indicating the insoluble nature of PHATN at

different conditions, thus contributing to the stable long-term cycling. Even with high mass loading of 5 and 10 mg cm⁻², PHATN retains the high capacity of 163 and 145 mAh g⁻¹, respectively, after 500 cycles at 1 Ag⁻¹ (Supporting Information, Figure S9). Based on the mass loading of 5 mg cm⁻² and the corresponding thickness (ca. 9.83 μm; Supporting Information, Figure S10) of PHATN cathode, the volumetric and gravimetric energy densities of PHATN cathode are calculated to be 1.66 Wh cm⁻³ and 326 Wh kg⁻¹, respectively. To highlight the impact of high-concentration electrolyte (4 M NaPF₆ in DME) on cycling performance, PHATN in traditional electrolyte (1 M NaPF₆ in DME) was also evaluated, in which the capacity only remains at 120 mAh g⁻¹ (66.7 % of the initial capacity) after 800 cycles (Supporting Information, Figure S11), much worse than that in high-concentration electrolyte.

The sodiation/de-sodiation mechanism of PHATN was investigated using ex situ X-ray photoelectron spectroscopy (XPS; Figure 3a–c), where the C 1s peak at 284.8 eV in pristine PHATN is used as a reference binding energy (Supporting Information, Figure S13). The characteristic N 1s peak of pristine PHATN at 398.8 eV (Figure 3a) represents the –C=N–,^[27b] while the small peak at 400.4 eV stands for the –C–N–. When discharged to 1.0 V (Figure 3b), the peak for –C=N– is remarkably decreased, due to the reduction of –C=N– during the sodiation process, while a new peak at 398.6 eV stands for Na–N appears.^[32] After recharged to 3.5 V (Figure 3c), the de-sodiation leads to the recovery of the –C=N– peak and disappearance of Na–N peak, indicating the reversible sodiation and de-sodiation of –C=N– in PHATN. Apart from XPS, ex situ FTIR (Figure 3d) and Raman spectroscopy (Figure 3e) were also performed to study the sodiation and de-sodiation process of PHATN. The

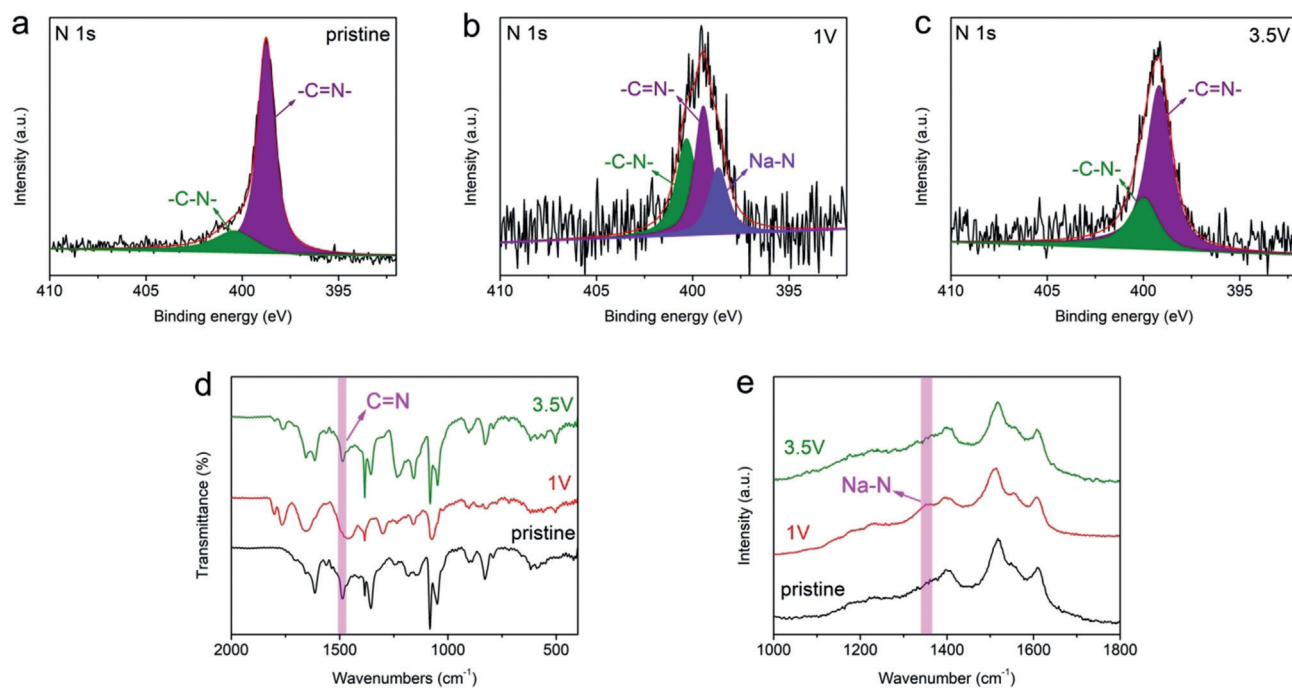


Figure 3. The investigation of reaction mechanism of PHATN in NIBs. a)–c) XPS N 1s, d) FTIR spectra, and e) Raman spectra of PHATN in various states: pristine, discharged to 1 V, and recharged to 3.5 V.

strong vibration absorption peak at around 1495 cm^{-1} , assigned to the C=N- of imine groups,^[27a] almost disappears after discharged to 1 V (Figure 3d). When recharged to 3.5 V, the peak recovers, indicating the C=N- sites of imine groups are the redox-active center of PHATN. In Raman spectra (Figure 3e), when PHATN is fully discharged to 1 V, a peak at 1352 cm^{-1} , representing the sodiated imine group (Na-N), appears, demonstrating the imine groups react with Na ions during the sodiation process. When recharged to 3.5 V, the Na-N peak disappears, demonstrating the reversible electrochemical reaction between the imine group and Na ion. Furthermore, the reversible sodiation and de-sodiation of PHATN is also confirmed by energy-dispersive X-ray spectroscopy (EDS; Supporting Information, Figure S14).

Magnesium/De-magnesium and Al-Ion Insertion/Extraction Performance of PHATN

The superfast sodiation and de-sodiation kinetics motivates us to see if the fast kinetics of PHATN in NIBs would translate to superior performance in RMBs and RABs. In PHATN/Mg pouch cells, the initial discharge/charge curves show a discharge capacity of 146 mAh g^{-1} with the plateau of 1.5 V, and a charge capacity of 156 mAh g^{-1} with the plateau of 1.75 V (Figure 4a). These values are in good agreement

with the predicted redox potential of 1.83 V from periodic DFT calculations and 1.2–1.8 V from the cluster continuum calculations for $\text{Mg}(\text{HATN})_2$ in the Supporting Information, Tables S3 and S4. In RABs, the first discharge delivers a capacity of 145 mAh g^{-1} with a plateau at 0.7 V, followed by a charge capacity of 125 mAh g^{-1} with a plateau at 0.9–1.0 V, corresponding to CE of 86.2 % (Figure 4b). The overpotential between discharge and charge process is 0.2–0.3 V (Figure 4b), lower than many inorganic cathodes for RABs.^[9b,11b,33] In the long-term cycling test, PHATN/Mg full cells can maintain a reversible capacity of 110 mAh g^{-1} for 200 cycles with CE close to 100 % (Figure 4c), while in RABs PHATN maintains a capacity of 92 mAh g^{-1} after 100 cycles with CE of around 99.7 % (Figure 4d), indicating the good stability of PHATN in both RMBs and RABs. The rate capability of PHATN in RMBs was evaluated at various current densities. When the current density increases from C/10 to 1C, capacities of PHATN decrease from 125 to 60 mAh g^{-1} (Figure 4e), showing a better rate performance than most inorganic cathode materials in RMBs.^[11a,34] The reaction kinetics of PHATN was further evaluated by GITT. The cell was charged/discharged for 1 h at 20 mA g^{-1} , and then relaxed for 1 h to reach the equilibrium potentials (Figure 4f). Apparently, the overpotential during discharge (ca. 0.11 V) is smaller than that during charge (ca. 0.49 V), indicating the faster kinetics for magnesiation process, which is common for cathodes in RMBs.^[6a,8b,34d]

The magnesiation/de-magnesiation mechanism of PHATN was investigated using ex situ XPS, FTIR, and Raman spectra (Figure 5; Supporting Information, Figure S16). When discharged to 0.5 V (Figure 5a), the peak for C=N- is remarkably reduced, owing to the reduction of C=N- in the magnesiation process, while a new peak at 398.0 eV representing Mg-N appears.^[32a-c] After recharged to 2.3 V (Figure 5b), the de-magnesiation leads to the recovery of the C=N- peak and disappearance of Mg-N peak, indicating the reversible magnesiation and de-magnesiation of C=N- in PHATN. For FTIR, a strong vibration absorption

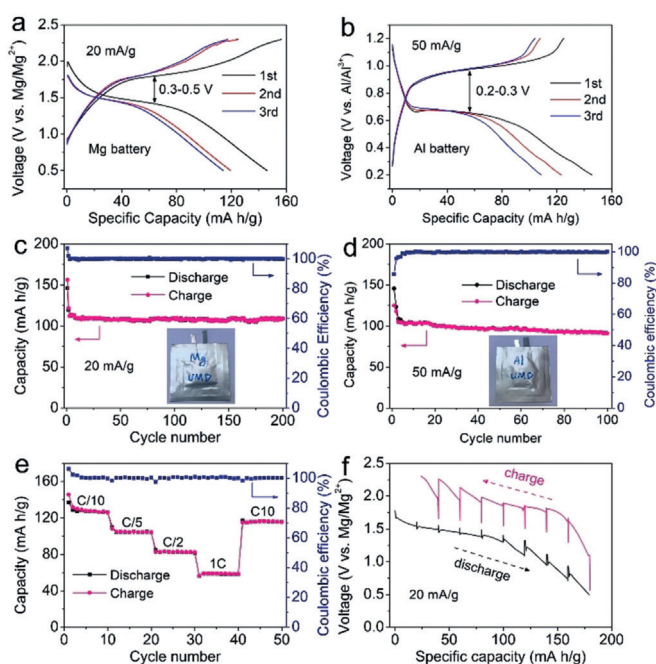


Figure 4. Electrochemistry of PHATN in RMBs with a Mg negative electrode between 0.5 and 2.3 V, and in RABs with the $\text{AlCl}_3\text{-[BMIm]Cl}$ ionic liquid electrolyte and an Al negative electrode between 0.2 and 1.2 V at RT. The discharge-charge curves for the first three cycles a) in RMBs at 20 mA g^{-1} and b) in RABs at 50 mA g^{-1} . Cycling performance and coulombic efficiency (CE) of c) the first 200 cycles at 20 mA g^{-1} in RMBs and d) the first 100 cycles at 50 mA g^{-1} in RABs. e) Rate capabilities of PHATN in RMBs at various current rates from C/10 to 1C. f) Quasi-equilibrium voltage profile of PHATN/Mg system obtained from GITT. The cells were allowed to relax for 1 h after every 1 h discharging or charging at 20 mA g^{-1} .

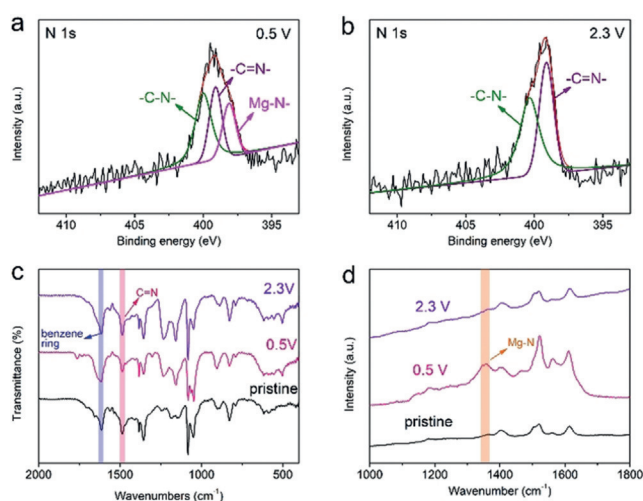


Figure 5. The investigation of reaction mechanism of PHATN in RMBs. a), b) XPS N 1s, c) FTIR, and d) Raman spectra of PHATN in various states: pristine, fully discharged to 0.5 V, and fully recharged to 2.3 V.

peak at around 1495 cm^{-1} is assigned to the $\text{C}=\text{N}$ of imine groups (Figure 5c). Compared to benzene ring at 1615 cm^{-1} , the intensity of $\text{C}=\text{N}$ peak remarkably decreases when discharged to 1 V, which recovers after recharged to 2.3 V, indicating the $\text{C}=\text{N}$ sites of imine groups are the redox-active center of PHATN. The Raman spectroscopy was also performed to study the magnesiation and de-magnesiation process of PHATN (Figure 5d), and compared to calculated Raman spectra with Mg coordination using DFT by progressively increasing the number of Mg in the Mg_xHATN complexes as shown in the Supporting Information, Figure S17. For isolated $\text{Mg}_3(\text{HATN})_4$, the emergence of a broad peak spanning from 1250 to 1350 cm^{-1} , which is well match with a broad peak at around 1350 cm^{-1} from recorded spectra of discharged PHATN, is a good probe of Mg–N bond formation (Supporting Information, Figure S17). Then, recharged to 2.3 V, Raman spectra recover to the pristine one (Figure 5d), indicating the highly reversible magnesiation of PHATN. Therefore, ex situ XPS, FTIR, Raman spectroscopy, and DFT calculation results confirm that the pyrazine functional groups are the multiple redox centers for magnesiation and de-magnesiation of PHATN. Energy-dispersive X-ray spectroscopy (EDS) was conducted to investigate the Al-ion insertion and extraction mechanism of PHATN (Supporting Information, Figure S18). Four electrodes on different discharged/charged states indicate the presence of both aluminum and chlorine. The Al-to-Cl atomic ratios obtained from various spots support an AlCl_2^+ storage mechanism. In other words, it is AlCl_2^+ , instead of Al^{3+} , that reacts with $\text{C}=\text{N}$ redox-active centers, which has also been demonstrated by other organic cathodes in RABs.^[35]

Conclusion

In this work, we applied a polymer (PHATN) in which the redox-active centers are based on multi-electron-deficient pyrazine sites as a universal cathode for NIBs, RMBs, and RABs. In NIBs, PHATN cathodes achieve fast reaction kinetics, ultra-stable cycling, and high energy density. At 2 A g^{-1} (5C), it renders a capacity of 165 mAh g^{-1} after 10000 cycles. Even at ultrahigh current density of 10 A g^{-1} (25C), PHATN still maintains 100 mAh g^{-1} after 50000 cycles. Such high capacity delivery and retention, as far as we know, are the highest among polymer and inorganic cathodes for NIBs. In RMBs and RABs, PHATN also renders stable cycling performance and fast reaction kinetics, in which it delivers the capacities of 110 and 92 mAh g^{-1} after 200 and 100 cycles in RMBs and RABs, respectively. XPS, FTIR, Raman, and DFT calculations are employed to demonstrate that the redox-active sites are based on the highly reversible pyrazine groups in PHATN. This work proves that the pyrazine-based polymer cathode is promising for developing environmentally benign, high-energy-density, fast and ultra-stable rechargeable batteries.

Acknowledgements

We thank Dr. Karen J. Gaskell at the Surface Analysis Center of University of Maryland for the help on the XPS test and data analysis. The authors also thank Wenzhuo Cao from Institute of Physics, Chinese Academy of Sciences for the help on mass spectra. This work was supported by the US National Science Foundation Award No.: 1438198. The authors also acknowledge the support from the Nanostructures for Electrical Energy Storage (NEES), an Energy Frontier Research Center funded by the US Department of Energy, Office of Science, Basic Energy Sciences, under Award number DESC0001160. M.M.'s fellowship was supported by China Scholarship Council (grant no. 201606130050). This work was also supported by the National Natural Science Foundation of China (grant no. 21905299) and China Postdoctoral Science Foundation (2019TQ0346).

Conflict of interest

The authors declare no conflict of interest.

Keywords: fast charging · polymer cathodes · rechargeable Al batteries · rechargeable Mg batteries · sodium ion batteries

How to cite: *Angew. Chem. Int. Ed.* **2019**, *58*, 17820–17826
Angew. Chem. **2019**, *131*, 17984–17990

- [1] a) B. Dunn, H. Kamath, J.-M. Tarascon, *Science* **2011**, *334*, 928–935; b) Z. Yang, J. Zhang, M. C. W. Kintner-Meyer, X. Lu, D. Choi, J. P. Lemmon, J. Liu, *Chem. Rev.* **2011**, *111*, 3577–3613.
- [2] a) J. F. Parker, C. N. Chervin, I. R. Pala, M. Machler, M. F. Burz, J. W. Long, D. R. Rolison, *Science* **2017**, *356*, 415–418; b) J. W. Choi, D. Aurbach, *Nat. Rev. Mater.* **2016**, *1*, 16013.
- [3] a) N. Yabuuchi, K. Kubota, M. Dahbi, S. Komaba, *Chem. Rev.* **2014**, *114*, 11636–11682; b) K. Sung-Wook, S. Dong-Hwa, M. Xiaohua, C. Gerbrand, K. Kisuk, *Adv. Energy Mater.* **2012**, *2*, 710–721.
- [4] a) M. Mao, F. Yan, C. Cui, J. Ma, M. Zhang, T. Wang, C. Wang, *Nano Lett.* **2017**, *17*, 3830–3836; b) M. Mao, C. Cui, M. Wu, M. Zhang, T. Gao, X. Fan, J. Chen, T. Wang, J. Ma, C. Wang, *Nano Energy* **2018**, *45*, 346–352; c) L. Wang, Z. Wei, M. Mao, H. Wang, Y. Li, J. Ma, *Energy Storage Mater.* **2019**, *16*, 434–454; d) X. Xie, M. Mao, S. Qi, J. Ma, *CrystEngComm* **2019**, *21*, 3755–3769.
- [5] a) M. S. Whittingham, *Chem. Rev.* **2014**, *114*, 11414–11443; b) J.-M. Tarascon, M. Armand, *Materials for Sustainable Energy*, Springer, Heidelberg, **2010**, pp. 171–179.
- [6] a) M. M. Huie, D. C. Bock, E. S. Takeuchi, A. C. Marschillo, K. J. Takeuchi, *Coord. Chem. Rev.* **2015**, *287*, 15–27; b) P. Saha, M. K. Datta, O. I. Velikokhatnyi, A. Manivannan, D. Alman, P. N. Kumta, *Prog. Mater. Sci.* **2014**, *66*, 1–86; c) F. Ambroz, T. J. Macdonald, T. Nann, *Adv. Energy Mater.* **2017**, *7*, 1602093.
- [7] a) O. Mizrahi, N. Amir, E. Pollak, O. Chusid, V. Marks, H. Gottlieb, L. Larush, E. Zinigrad, D. Aurbach, *J. Electrochem. Soc.* **2008**, *155*, A103–A109; b) T. Jiang, M. J. Chollier Brym, G. Dubé, A. Lasia, G. M. Brisard, *Surf. Coat. Technol.* **2006**, *201*, 1–9; c) M. Mao, T. Gao, S. Hou, F. Wang, J. Chen, Z. Wei, X. Fan, X. Ji, J. Ma, C. Wang, *Nano Lett.* **2019**, *19*, 6665–6672.

- [8] a) H. D. Yoo, I. Shterenberg, Y. Gofer, G. Gershinsky, N. Pour, D. Aurbach, *Energy Environ. Sci.* **2013**, 6, 2265–2279; b) J. Muldoon, C. B. Bucur, T. Gregory, *Chem. Rev.* **2014**, 114, 11683–11720; c) T. Gao, S. Hou, K. Huynh, F. Wang, N. Eidson, X. Fan, F. Han, C. Luo, M. Mao, X. Li, C. Wang, *ACS Appl. Mater. Interfaces* **2018**, 10, 14767–14776.
- [9] a) S. K. Das, S. Mahapatra, H. Lahan, *J. Mater. Chem. A* **2017**, 5, 6347–6367; b) Z. A. Zafar, S. Imtiaz, R. Razaq, S. Ji, T. Huang, Z. Zhang, Y. Huang, J. A. Anderson, *J. Mater. Chem. A* **2017**, 5, 5646–5660.
- [10] M. Mao, X. Ji, S. Hou, T. Gao, F. Wang, L. Chen, X. Fan, J. Chen, J. Ma, C. Wang, *Chem. Mater.* **2019**, 31, 3183–3191.
- [11] a) D. Aurbach, Z. Lu, A. Schechter, Y. Gofer, H. Gizbar, R. Turgeman, Y. Cohen, M. Moshkovich, E. Levi, *Nature* **2000**, 407, 724; b) L. Geng, G. Lv, X. Xing, J. Guo, *Chem. Mater.* **2015**, 27, 4926–4929.
- [12] a) T. B. Schon, B. T. McAllister, P.-F. Li, D. S. Seferos, *Chem. Soc. Rev.* **2016**, 45, 6345–6404; b) S. Muench, A. Wild, C. Friebe, B. Häupler, T. Janoschka, U. S. Schubert, *Chem. Rev.* **2016**, 116, 9438–9484.
- [13] a) X. Fan, F. Wang, X. Ji, R. Wang, T. Gao, S. Hou, J. Chen, T. Deng, X. Li, L. Chen, C. Luo, L. Wang, C. Wang, *Angew. Chem. Int. Ed.* **2018**, 57, 7146–7150; *Angew. Chem.* **2018**, 130, 7264–7268; b) B. Pan, J. Huang, Z. Feng, L. Zeng, M. He, L. Zhang, J. T. Vaughey, M. J. Bedzyk, P. Fenter, Z. Zhang, A. K. Burrell, C. Liao, *Adv. Energy Mater.* **2016**, 6, 1600140; c) M. Mao, T. Gao, S. Hou, C. Wang, *Chem. Soc. Rev.* **2018**, 47, 8804–8841.
- [14] a) Z. Song, H. Zhou, *Energy Environ. Sci.* **2013**, 6, 2280–2301; b) L. Yanliang, Z. Peng, Y. Siqi, T. Zhanliang, C. Jun, *Adv. Energy Mater.* **2013**, 3, 600–605.
- [15] T. S. Naidu, H. T. Hoon, J. S. Hyun, B. Onur, C. J. Wook, C. Ali, *Angew. Chem. Int. Ed.* **2016**, 55, 3106–3111; *Angew. Chem.* **2016**, 128, 3158–3163.
- [16] a) O. Kenichi, N. Hiroyuki, *Adv. Mater.* **2009**, 21, 2339–2344; b) T. Janoschka, M. D. Hager, U. S. Schubert, *Adv. Mater.* **2012**, 24, 6397–6409.
- [17] B. Häupler, A. Wild, U. S. Schubert, *Adv. Energy Mater.* **2015**, 5, 1402034.
- [18] a) J. Hong, M. Lee, B. Lee, D.-H. Seo, C. B. Park, K. Kang, *Nat. Commun.* **2014**, 5, 5335; b) T. B. Schon, A. J. Tilley, C. R. Bridges, M. B. Miltenburg, D. S. Seferos, *Adv. Funct. Mater.* **2016**, 26, 6896–6903.
- [19] a) C. Luo, X. Ji, S. Hou, N. Eidson, X. Fan, Y. Liang, T. Deng, J. Jiang, C. Wang, *Adv. Mater.* **2018**, 30, 1706498; b) C. Luo, O. Borodin, X. Ji, S. Hou, K. J. Gaskell, X. Fan, J. Chen, T. Deng, R. Wang, J. Jiang, C. Wang, *Proc. Natl. Acad. Sci. USA* **2018**, 115, 2004–2009.
- [20] a) D. Chen, A.-J. Avestro, Z. Chen, J. Sun, S. Wang, M. Xiao, Z. Erno, M. M. Algaradah, M. S. Nassar, K. Amine, Y. Meng, J. F. Stoddart, *Adv. Mater.* **2015**, 27, 2907–2912; b) T. Nokami, T. Matsuo, Y. Inatomi, N. Hojo, T. Tsukagoshi, H. Yoshizawa, A. Shimizu, H. Kuramoto, K. Komae, H. Tsuyama, J.-i. Yoshida, *J. Am. Chem. Soc.* **2012**, 134, 19694–19700; c) Z. Song, Y. Qian, M. L. Gordin, D. Tang, T. Xu, M. Otani, H. Zhan, H. Zhou, D. Wang, *Angew. Chem. Int. Ed.* **2015**, 54, 13947–13951; *Angew. Chem.* **2015**, 127, 14153–14157.
- [21] S. Zhiping, Z. Hui, Z. Yunhong, *Angew. Chem. Int. Ed.* **2010**, 49, 8444–8448; *Angew. Chem.* **2010**, 122, 8622–8626.
- [22] a) Q. Zhao, Y. Lu, J. Chen, *Adv. Energy Mater.* **2017**, 7, 1601792; b) Q. Zhao, J. Wang, Y. Lu, Y. Li, G. Liang, J. Chen, *Angew. Chem. Int. Ed.* **2016**, 55, 12528–12532; *Angew. Chem.* **2016**, 128, 12716–12720; c) C. Luo, X. Fan, Z. Ma, T. Gao, C. Wang, *Chem* **2017**, 3, 1050–1062; d) M. Lee, J. Hong, D.-H. Seo, D. H. Nam, K. T. Nam, K. Kang, C. B. Park, *Angew. Chem. Int. Ed.* **2013**, 52, 8322–8328; *Angew. Chem.* **2013**, 125, 8480–8486.
- [23] Y. Huang, C. Fang, W. Zhang, Q. Liu, Y. Huang, *Chem. Commun.* **2019**, 55, 608–611.
- [24] Y. Kou, Y. Xu, Z. Guo, D. Jiang, *Angew. Chem. Int. Ed.* **2011**, 50, 8753–8757; *Angew. Chem.* **2011**, 123, 8912–8916.
- [25] a) N. Kentaro, O. Kenichi, N. Hiroyuki, *Chem. Lett.* **2011**, 40, 222–227; b) Y. Hanyu, T. Sugimoto, Y. Ganbe, A. Masuda, I. Honma, *J. Electrochem. Soc.* **2014**, 161, A6–A9.
- [26] F. Xu, X. Chen, Z. Tang, D. Wu, R. Fu, D. Jiang, *Chem. Commun.* **2014**, 50, 4788–4790.
- [27] a) S. Xu, G. Wang, B. P. Biswal, M. Addicoat, S. Paasch, W. Sheng, X. Zhuang, E. Brunner, T. Heine, R. Berger, X. Feng, *Angew. Chem. Int. Ed.* **2019**, 58, 849–853; *Angew. Chem.* **2019**, 131, 859–863; b) J. Wang, C. S. Chen, Y. Zhang, *ACS Sustainable Chem. Eng.* **2018**, 6, 1772–1779.
- [28] K. Momma, F. Izumi, *J. Appl. Crystallogr.* **2011**, 44, 1272–1276.
- [29] a) D. Tomerini, O. Politano, C. Gatti, C. Frayret, *Phys. Chem. Chem. Phys.* **2016**, 18, 26651–26660; b) Y. Chen, J. Lüder, M.-F. Ng, M. Sullivan, S. Manzhos, *Phys. Chem. Chem. Phys.* **2018**, 20, 232–237; c) K. C. Kim, T. Liu, S. W. Lee, S. S. Jang, *J. Am. Chem. Soc.* **2016**, 138, 2374–2382.
- [30] K. Okhotnikov, T. Charpentier, S. Cadars, *J. Cheminf.* **2016**, 8, 17.
- [31] a) F. Xu, H. Wang, J. Lin, X. Luo, S.-a. Cao, H. Yang, *J. Mater. Chem. A* **2016**, 4, 11491–11497; b) Y. Wang, Y. Ding, L. Pan, Y. Shi, Z. Yue, Y. Shi, G. Yu, *Nano Lett.* **2016**, 16, 3329–3334; c) C. Luo, J. Wang, X. Fan, Y. Zhu, F. Han, L. Suo, C. Wang, *Nano Energy* **2015**, 13, 537–545; d) H.-g. Wang, S. Yuan, D.-l. Ma, X.-l. Huang, F.-l. Meng, X.-b. Zhang, *Adv. Energy Mater.* **2014**, 4, 1301651.
- [32] a) Z. H. Ma, S. L. Lim, K. L. Tan, S. Li, E. T. Kang, *Surf. Sci.* **2000**, 454–456, 995–999; b) P. Xie, M. Z. Rong, M. Q. Zhang, *Angew. Chem. Int. Ed.* **2016**, 55, 1805–1809; *Angew. Chem.* **2016**, 128, 1837–1841; c) R. Rajagopalan, J. O. Iroh, *Appl. Surf. Sci.* **2003**, 218, 58–69; d) Y. Liang, Y. Jing, S. Gheytani, K.-Y. Lee, P. Liu, A. Facchetti, Y. Yao, *Nat. Mater.* **2017**, 16, 841.
- [33] S. Wang, S. Jiao, J. Wang, H.-S. Chen, D. Tian, H. Lei, D.-N. Fang, *ACS Nano* **2017**, 11, 469–477.
- [34] a) X. Sun, P. Bonnick, L. F. Nazar, *ACS Energy Lett.* **2016**, 1, 297–301; b) P. Bonnick, L. Blanc, S. H. Vajargah, C.-W. Lee, X. Sun, M. Balasubramanian, L. F. Nazar, *Chem. Mater.* **2018**, 30, 4683–4693; c) X. Sun, P. Bonnick, V. Duffort, M. Liu, Z. Rong, K. A. Persson, G. Ceder, L. F. Nazar, *Energy Environ. Sci.* **2016**, 9, 2273–2277; d) F. Xiong, Y. Fan, S. Tan, L. Zhou, Y. Xu, C. Pei, Q. An, L. Mai, *Nano Energy* **2018**, 47, 210–216.
- [35] D. J. Kim, D.-J. Yoo, M. T. Otley, A. Prokofjevs, C. Pezzato, M. Owczarek, S. J. Lee, J. W. Choi, J. F. Stoddart, *Nat. Energy* **2019**, 4, 51–59.

Manuscript received: August 26, 2019

Accepted manuscript online: September 30, 2019

Version of record online: October 23, 2019